

Optics Letters

Label-free brainwide visualization of senile plaque using cryo-micro-optical sectioning tomography

YILIN LUO,^{1,2,†} ANLE WANG,^{1,2,3,†} MENG MENG LIU,^{1,2} TIAN LEI,^{1,2} XIAOCHUAN ZHANG,⁴  ZHAOBING GAO,⁴ 
HUALIANG JIANG,⁴ HUI GONG,^{1,2} AND JING YUAN^{1,2,*} 

¹Britton Chance Center for Biomedical Photonics, Wuhan National Laboratory for Optoelectronics-Huazhong University of Science and Technology, Wuhan, Hubei 430074, China

²MoE Key Laboratory for Biomedical Photonics, Collaborative Innovation Center for Biomedical Engineering, School of Engineering Sciences, Huazhong University of Science and Technology, Wuhan, Hubei 430074, China

³Current address: Air Force Early Warning Academy, Wuhan, Hubei 430017, China

⁴State Key Laboratory of Drug Research, CAS Key Laboratory of Receptor Research, Shanghai Institute of Materia Medica, Chinese Academy of Sciences, Shanghai 201203, China

*Corresponding author: yuanj@hust.edu.cn

Received 1 August 2017; revised 13 September 2017; accepted 13 September 2017; posted 18 September 2017 (Doc. ID 303420); published 18 October 2017

Optical visualization of pathological changes in Alzheimer's disease (AD) can facilitate exploration of disease mechanisms and treatments. However, existing optical imaging methods have limitations on mapping pathological evolution in the whole mouse brain. Previous research indicated endogenous fluorescence contrast of senile plaques. Therefore, we develop cryo-micro-optical sectioning tomography (cryo-MOST) to capture intrinsic fluorescence distribution of senile plaques at a micrometer-level resolution in the whole brain. Validation using immunofluorescence demonstrates the capacity of cryo-MOST to visualize and distinguish senile plaques with competent sensitivity and spatial resolution. Compared with imaging in room temperature, cryo-MOST provides better signal intensity and signal-to-noise ratio. Using cryo-MOST, we obtained whole-brain coronal distribution of senile plaques in a transgenic mouse without exogenous dye. Capable of label-free brainwide visualization of Alzheimer's pathology, cryo-MOST may be potentially useful for understanding neurodegenerative disease mechanisms and evaluating drug efficacy. © 2017 Optical Society of America

OCIS codes: (170.3880) Medical and biological imaging; (170.6900) Three-dimensional microscopy; (170.2520) Fluorescence microscopy; (170.4730) Optical pathology.

<https://doi.org/10.1364/OL.42.004247>

Senile plaque is one of the two primary pathological characteristics of Alzheimer's disease (AD). These amyloid plaques abnormally accumulate in specific brain regions such as temporal lobe in early disease stage and spread across the entire brain along disease progression [1]. To investigate disease mechanisms and treatments, multiple imaging modalities have been developed to visualize plaque distribution in brain. Positron

emission tomography (PET) is capable of imaging *in vivo* amyloid accumulation in human and transgenic mouse models after intravenous administration of tracer Pittsburgh Compound-B (PIB) [2,3]. Magnetic resonance imaging (MRI) has been developed to visualize senile plaques noninvasively without a contrast agent [4]. However, these imaging techniques are limited by their low spatial resolution and contrast in the application of detecting microscopic neuropathologic progression. To capture these subtle changes, some optical methods have been developed. Photoacoustic microscopy provides *in vivo* visualization of plaque deposits with optical resolution and sound penetration depth [5], but it requires specific exogenous dyes to enhance the signal-to-noise ratio (SNR), which may disrupt tissue metabolic activities. *In vivo* multiphoton microscopy, combined with second harmonic generation (SHG) microscopy, has been demonstrated to provide sub-micrometer-resolution observation on senile plaques using intrinsic emissions [6]. Nevertheless, its imaging depth is limited to brain surface or brain slices and is thus unable to provide brain-wide mapping of plaque distribution. Therefore, no method is available for acquiring the distribution of senile plaques at a micrometer-scale resolution in the whole brain without exogenous dyes.

In this Letter, we present cryo-micro-optical sectioning tomography (cryo-MOST) to acquire the brainwide mapping of senile plaques using intrinsic fluorescence emission. We overlapped cryo-MOST autofluorescence images with immunofluorescence images to validate imaging capability. Autofluorescence images acquired in low and room temperature were directly compared to examine the SNR improvement of our system. We also verified that senile plaques were visualized free from the potential interference from flavin adenine dinucleotide (FAD) background autofluorescence in brain tissue. Furthermore, a series of coronal distributions of Alzheimer's pathology in the whole transgenic mouse brain were mapped by cryo-MOST. We demonstrate that this technology enables label-free optical visualization of senile plaques in the whole mouse brain.

Figure 1 shows a configuration of the cryo-MOST system. The system consists of an optical imaging module (MVX10, Olympus), a low-temperature sample box, a miller machine, and an XZ stage. Considering damage from low-temperature environment on objective lens, we use stereomicroscopy due to its microscopic imaging capability and long working distance. Excitation light generated by Halogen lamp (Olympus) is directed through a 434 nm bandpass filter of 17 nm bandwidth (FF01-434/17, Semrock) and focused on the back focal plane of an objective lens. The filtered light is deflected by a dichroic mirror of 510 nm (FF510-Di02, Semrock) into a 0.25 NA objective lens (MVPLAPO 1 \times , Olympus) to be focused on the sample surface. Epi-fluorescence signals are collected by the objective lens and transmitted into detection channel by the dichroic mirror. After passing through another lens followed by a 536 nm bandpass filter of 40 nm bandwidth (FF01-536/40, Semrock), the fluorescence image on the XY plane is finally relayed to a camera (Flash 2.8 C11440-10C, Hamamatsu). We follow an improved directional funnel freezing protocol [7] to cryo-fix the whole mouse brain. We put an 8.8 mm bottom diameter funnel over the skull and pour liquid nitrogen into the funnel. Then we wait for over 3 min to obtain full cyrofixation in the mouse brain. The specimen is then embedded into a customized sample tube (not shown for simplicity) using embedding medium (10% ethanol, 30% glycerol, and 60% deionized water). The tube is placed in the low-temperature sample box, and the specimen is immersed in liquid nitrogen to maintain a temperature lower than -100°C at the imaging surface. The working distance of more than 20 mm allows the objective lens to keep normal working temperature. A miller machine (A3, Sanyou) performs automated sectioning by polishing the imaged top surface of the specimen. Before each imaging, we perform a quick oblique jet of liquid nitrogen to eliminate residual debris and keep the surface smooth. The XZ stage moves the specimen in the X direction for imaging and in the Z direction to perform the next milling operation. The system performs alternating milling and imaging in an automated fashion. If needed, a cryo-MOST system can function in white-light reflecting mode by removing filters and replacing the dichroic mirror with a beam splitter.

To validate imaging capability of the cryo-MOST for senile plaques, we compared low-temperature autofluorescence signals with conventional amyloid- β -specific immunofluorescence images. Three 10-month-old male APP/PS1 (Jackson Laboratory, USA) mice were fixed by standard vascular

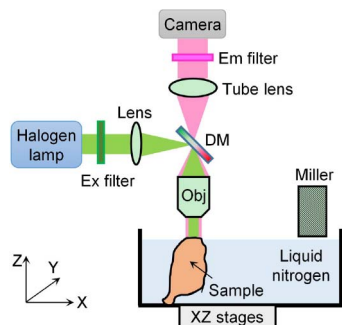


Fig. 1. Schematic of the cryo-MOST. Obj, objective lens; DM, dichroic mirror; Ex, excitation; Em, emission. The sample tube is not drawn for simplicity.

perfusion fixation process. All of the animal experiments were approved by the Institutional Animal Ethics Committee of Huazhong University of Science and Technology, and all experiments were performed in accordance with relevant guidelines and regulations. We continuously sectioned the mice brains along anterior-posterior axis at a thickness of 40 μm and randomly selected 10 slices containing hippocampus from each mouse for subsequent labeling. These slices were labeled by 6E10, a monoclonal antibody specific for amyloid- β amino acid residue A β 1–16 [8]. The antibodies were tagged by fluorescein Alexa 594 (Life Technologies). All slices were sealed by 80% w/v glycerol diluted in 0.01 M PBS to prevent frost crack under low temperature. The imaged slice was placed 0.5 cm above a liquid nitrogen surface to avoid direct contact for the same reason. To image the immunofluorescence labels, a group of extra excitation/emission filters (FF01-470/28, Semrock: 470 nm excitation bandpass filter of 22 nm bandwidth and FF01-680/22, Semrock: 680 nm emission bandpass filter of 22 nm bandwidth) were implemented in the system. We acquired intrinsic and extrinsic fluorescence images sequentially by switching the filter groups for each slice. The exposure time was 5 s for both channels. Figures 2(a) and 2(b) show an intrinsic fluorescence image and an immunofluorescence-labeled image of a typical half hippocampal coronal plane. In Fig. 2(a), we can clearly distinguish plaque-like autofluorescence signals. Senile plaque immunofluorescence in Fig. 2(b) highly overlapped with these signals, which confirmed that they were from senile plaques. In contrast, an image of a wild-type C57 mouse showed no plaque signal in the same imaging condition [Fig. 2(c)]. The observation demonstrated that senile plaque is the typical pathological characteristic of AD model. Figure 2(d) displayed an overlapped image of the intrinsic and extrinsic fluorescence. The enlarged views of a 1×1 mm yellow dashed box indicated in Figs. 2(a), 2(b), and 2(d) were displayed in Figs. 2(e)–2(g), respectively, for better comparison. Almost all of the plaque signals were distinguished in both

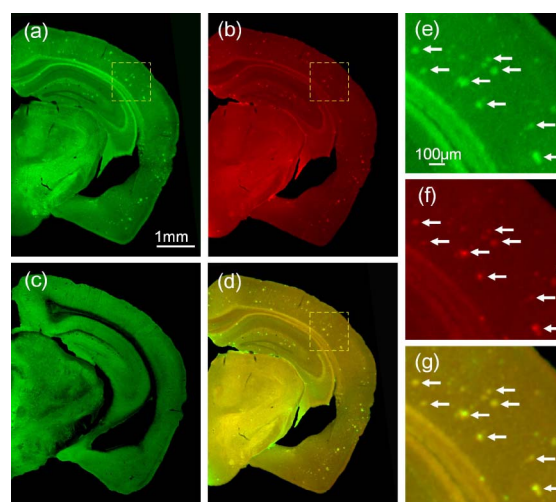


Fig. 2. Low temperature images of a typical half hippocampal coronal plane from a 10-month-old APP/PS1 mouse (pseudo colors). (a) Autofluorescence; (b) immunohistochemistry for comparison; (c) autofluorescence from a wild-type C57 mouse brain; (d) overlap of (a) and (b); (e)–(g) enlarged views from the dashed box in (a), (b), and (d), respectively.

the intrinsic channel and immunofluorescence channel [indicated by white arrows in Figs. 2(e)–2(g)]. Raw images were binarized and went through erosion and dilation operations to exclude the counting interference from lipofuscin of a size less than 5×5 pixels. Two persons back-to-back counted the plaques in all images to guarantee counting accuracy. The double-positive probability was calculated by the ratio of overlapped plaque number to immunofluorescence total plaque number. The result was 0.91 from statistics of 30 slices. High overlap shows that the intrinsic fluorescence acquired by cryo-MOST has adequate specificity and spatial resolution to identify amyloid plaques compared with immunohistochemistry.

To evaluate the SNR improvement of cryo-MOST, we directly compared autofluorescence images acquired in low and room temperature. We immersed a cryo-fixed 16-month-old APP/PS1 mouse brain in liquid nitrogen to obtain a cryo-image of the hippocampus coronal at the exposure time of 0.2 s [Fig. 3(a)]. Then cryo-MOST stopped data acquisition to wait for complete volatilization of liquid nitrogen. Another image [Fig. 3(b)] was recorded when the sample warmed up to room temperature. To capture autofluorescence in room temperature, we used the same exposure time. The cryo-image showed a clear brain coronal plane from which we could easily identify senile plaques in different brain regions. While even extending the exposure time, we acquired only a faint contour from the room-temperature image. The morphological characteristics of senile plaques could hardly be distinguished. Furthermore, the average autofluorescence intensities of these two images were 2042.9 and 345.8, respectively. The remarkable elevation of signal intensity benefited from quantum yield enhancement of intrinsic fluorescence under ultralow temperature [9]. This enhancement guarantees sufficient sensitivity of cryo-MOST on detecting autofluorescence signals from senile plaques. In addition, brain coronal images in Fig. 3(a) show that images obtained by the cryo-MOST suffered almost no tissue damage or morphological deformation compared with traditional histology. Intact images will facilitate our correct understanding of the position and distribution of senile plaques in the brain.

Because senile plaque has the same autofluorescence detection channel as FAD, which is an oxidation indicator of redox state, we measured and compared emission spectrums of both components. Then we evaluated whether FAD autofluorescence interfered with senile plaque detection. We acquired an autofluorescence image of an unstained brain slice from a 17-month-old APP/PS1 mouse with a fluorescence microscope (FV1000, Olympus) in room temperature [Fig. 4(a)] and measured autofluorescence emission spectrums of two randomly selected senile plaques [Fig. 4(b)]. The emission spectrums were similar with the result of [6] by two-photon excitation. Then we measured the emission spectrum of 0.5 mmol/L

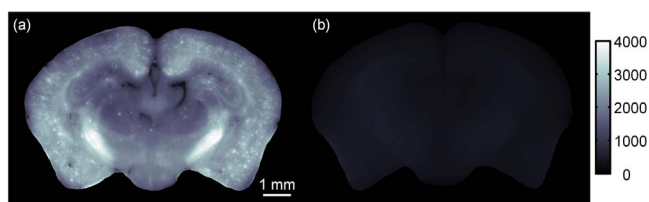


Fig. 3. Autofluorescence images of senile plaques in the hippocampal coronal plane from a 16-month-old APP/PS1 mouse brain by Cryo-MOST under (a) low temperature and (b) room temperature.

FAD solution (F6625, Sigma) with a VIS-NIR fiber spectrometer (USB-4000, Ocean Optics). Figure 4(b) shows high overlap of senile plaque and FAD autofluorescence at the emission peak, which indicates potential background interference. To evaluate this potential interference of redox measurement, we compared redox autofluorescence signals of nine-month-old APP/PS1 mouse brains in normoxia [Figs. 4(c) and 4(d)] and hypoxia [Figs. 4(e) and 4(f)] using cryo-MOST. To indicate the metabolism state, we measured autofluorescence from FAD and nicotinamide-adenine dinucleotide (NADH), which is another reduction indicator of the redox state. We added another group of excitation/emission filters (FF01-360/12, Semrock: 360 nm excitation bandpass filter of 12 nm bandwidth; FF01-470/28, Semrock: 470 nm emission bandpass filter of 28 nm bandwidth) and a dichroic mirror of 390 nm (FF390-Di01, Semrock) to measure NADH signal. Exposure time was 0.5 s for FAD channel and 0.2 s for NADH channel. All the other settings were the same. Intact cryo-fixation preparation enabled us to capture an accurate redox state. In hypoxia, N_2 euthanasia suffocated the mouse to death, which led to relatively lower oxidation [Fig. 4(e)] and much higher reduction of the redox state [Fig. 4(f)] compared with the normoxia state. The observation is consistent with that of a previous study [10]. In both FAD images [Figs. 4(c) and 4(e)], senile plaques were clearly distinguishable, and the average FAD background intensity was relatively low. To inhibit the potential interference from the FAD autofluorescence, we prefer sample preparation in hyperoxia.

Visualization of senile plaque 3D brainwide distribution is critical for understanding the pathology of Alzheimer's disease. To demonstrate our capability to obtain brainwide distribution

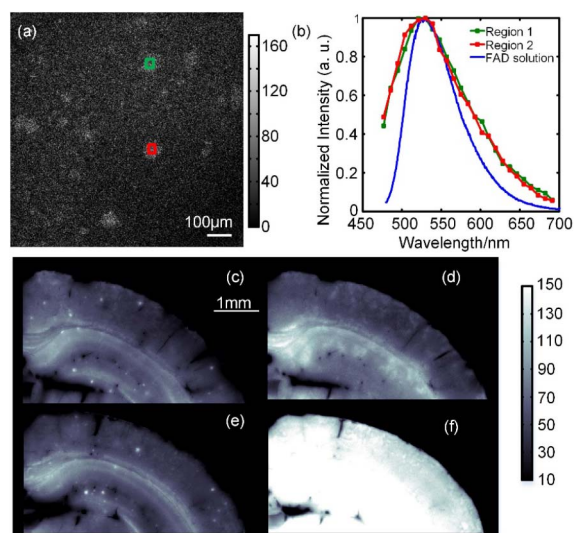


Fig. 4. Comparison of the autofluorescence of senile plaques and FAD. (a) Autofluorescence image of an unstained brain slice of a 17-month-old APP/PS1 mouse by fluorescence microscope (FV1000, Olympus) in room temperature. Red and green boxes indicated two randomly selected senile plaques, respectively; (b) normalized autofluorescence emission spectrums of two plaques indicated by the corresponding-color boxes in (a) and FAD solution (blue); autofluorescence images of hippocampal plane of a cryo-fixed normoxia nine-month-old APP/PS1 mouse brain in (c) FAD and (d) NADH channels; autofluorescence images of similar hippocampal plane of a hypoxia mouse brain in (e) FAD and (f) NADH channels.

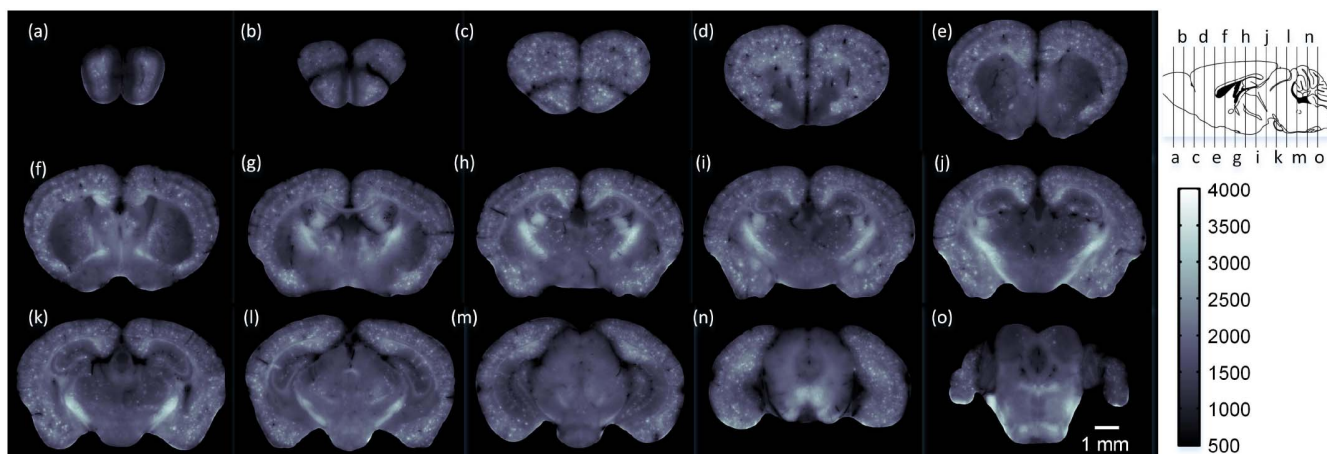


Fig. 5. Label-free brainwide map of senile plaque coronal distributions (a)–(o) obtained by cryo-MOST. Images were acquired from olfactory bulb to cerebellum with a 1 mm spacing. Specific locations are shown in the upper right inset.

of senile plaques, we imaged a whole 17-month APP/PS1 mouse brain using cryo-MOST. Figure 5 shows serial coronal autofluorescence images in the mouse brain. Images were obtained by sectioning along the anterior-posterior axis with a section thickness of 1 mm. No exogenous dye is used. Senile plaque distributions can be clearly visualized from olfactory bulb to cerebellum. Most plaques lay in cortex, some were distributed in hippocampus, and a minority spread to other areas. The plaques had spread to the whole brain. Furthermore, the plaque density of this 17-month AD transgenic mouse brain was much higher than that of the 10-month AD transgenic mouse brain in Fig. 2, which indicates an increase of amyloid aggregation along disease progression. Cryo-MOST, capable of surmounting optical depth limitation and obtaining senile plaque distribution in the whole brain, will be helpful in the study of AD brainwide pathological changes and drug efficacy evaluation. Our method provides a brand-new tool for this research.

In summary, we have described a cryo-MOST tomography to achieve a label-free brainwide visualization of senile plaques in AD transgenic mouse. Immediate freeze trapping of the mouse brain prevents tissue cellular structure from any morphological deformation. In the meantime, it simplifies the sample preparation process compared with immunohistochemistry. Moreover, an ultralow temperature environment enhances the tissue autofluorescence signal, allowing senile plaque imaging through endogenous fluorescence contrast. Finally, the mill-and-image working mode exceeds limitation on optical imaging depth, making label-free brainwide visualization of Alzheimer's pathology possible. Therefore, cryo-MOST may be a promising tool to investigate the brainwide pathological mechanisms of neurodegenerative diseases and to evaluate drug efficacy.

Although the current configuration of cryo-MOST has successfully achieved brainwide mapping of senile plaque distribution, image quality can be further improved. While stereomicroscopy provides long working distance in a low-temperature imaging environment, its lack of background inhibition severely degrades image quality. Employment of optical sectioning methods such as structured illumination microscopy will be helpful to visualize and distinguish plaques. In addition, current automation of the miller machine and XZ stage needs an upgrade to enhance milling and translation

accuracy. High precision will facilitate precise reconstruction of brainwide plaque distribution in high resolution and thus contributes to comprehensive analysis of senile plaque morphological characteristics.

Funding. Ministry of Science and Technology of the People's Republic of China (MOST) (2012YQ03026001, 2012YQ03026010); National Natural Science Foundation of China (NSFC) (61421064); Huazhong University of Science and Technology (HUST) (Director Fund of WNLO).

Acknowledgment. The authors appreciate the Optical Bioimaging Core Facility of WNLO-HUST for support in data acquisition and the Analytical and Testing Center of HUST for fluorescence imaging. We also thank Prof. Xiangning Li and Ben Long for assistance with immunostaining.

[†]These authors contributed equally to this work.

REFERENCES

1. H. Braak and E. Braak, *Acta Neuropathol.* **82**, 239 (1991).
2. J. Maeda, B. Ji, T. Irie, T. Tomiyama, M. Maruyama, T. Okauchi, M. Staufenbiel, N. Iwata, M. Ono, T. C. Saido, K. Suzuki, H. Mori, M. Hiquchi, and T. Suhara, *J. Neurosci.* **27**, 10957 (2007).
3. W. E. Klunk, H. Engler, A. Nordberg, Y. Wang, G. Blomqvist, D. P. Holt, M. Bergstrom, I. Savitcheva, G. Huang, S. Estrada, B. Ausen, M. L. Debnath, J. Barletta, J. C. Price, J. Sandell, B. J. Lopresti, A. Wall, P. Koivisto, G. Antoni, C. A. Mathis, and B. Langstrom, *Ann. Neurol.* **55**, 306 (2004).
4. C. R. Jack, Jr., M. Garwood, T. M. Wengenack, B. Borowski, G. L. Curran, J. Lin, G. Adriany, O. H. Grohn, R. Grimm, and J. F. Poduslo, *Magn. Reson. Med.* **52**, 1263 (2004).
5. S. Hu, P. Yan, K. Maslov, J. M. Lee, and L. V. Wang, *Opt. Lett.* **34**, 3899 (2009).
6. A. C. Kwan, K. Duff, G. K. Gouras, and W. W. Webb, *Opt. Express* **17**, 3679 (2009).
7. N. Sun, W. Luo, A. Wang, and Q. Luo, *Adv. Exp. Med. Biol.* **789**, 435 (2012).
8. D. R. Thakker, M. R. Weatherspoon, J. Harrison, T. E. Keene, D. S. Lane, W. F. Kaemmerer, G. R. Stewart, and L. L. Shafer, *Proc. Natl. Acad. Sci. USA* **106**, 4501 (2009).
9. J. R. Lakowicz, *Principles of Fluorescence Spectroscopy* (Springer, 2013).
10. B. Chance, P. Cohen, F. Jobsis, and B. Schoene, *Science* **137**, 660 (1962).